Defence Science Journal, Vol. 75, No. 6, November 2025, pp. 758-770, DOI : 10.14429/dsj.20786

Enhancing MEMS Gyroscope Performance with Vertical Sense Mass Design

Shaveta[#,*], R.K. Bhan[$] and Rishu Chaujar[!]

[#]*DRDO-Solid State Physics Laboratory, Timarpur, Delhi - 110 054, India*
[$]*DRDO-Institute of Defence Scientists and Technologists, Timarpur, Delhi - 110 054, India*
[!]*Delhi Technological University, Delhi - 110 042, India*
[*]*E-mail: shaveta.sspl@gov.in*

ABSTRACT

This study introduces a novel Vertical Sense Mass (VSM) design for MEMS gyroscope sensors, addressing the growing demand for miniaturization and enhanced performance in navigation and industrial applications. Leveraging Deep Reactive Ion Etching (DRIE) technology, the VSM design significantly reduces size while offering superior performance compared to traditional planar configurations. Comprehensive theoretical analysis and comparative evaluations demonstrate the VSM design's advantages across critical metrics, including sensitivity, bandwidth, noise, and device footprint. This advancement represents a substantial leap in MEMS gyroscope technology, enabling high-performance sensing in compact form factors. Specifically, the VSM design achieves a 30 % reduction in sense mass area, resulting in a 36 % smaller sensor footprint. This size reduction is coupled with a significant improvement in the overall Performance Metric (PM), with the VSM design exhibiting a PM of 1090 mHz/dps^{2}µm^2 compared to 70.7 mHz/dps^{2}µm^2 for the planar design. These analytical findings are supported by existing literature, further validating the superior performance of the proposed VSM design. The detailed fabrication process flow of the structure is presented, and successful fabrication of thick-proof-mass structures using DRIE confirms the feasibility of this innovative approach. These results highlight the potential of the VSM design for future applications requiring compact, high-performance gyroscope sensors.

Keywords: MEMS gyroscope; Vertical sense mass; Planar sense mass; Deep reactive ion etching; Performance metric; Mechanical sensitivity

1. INTRODUCTION

Bohenberger's gyroscopic machine, considered the first gyroscope, finds extensive application in various fields such as platform stabilisation, drone flight control, robotics, airbag rollover detection, smart ammunitions, satellite Inertial Measurement Units (IMUs), and sewerage network monitoring[1–8]. MEMS gyroscopes have significantly impacted inertial sensing due to their miniaturization, cost-effectiveness, and compatibility with integrated circuit technologies[9–15]. Conventional planar MEMS gyroscopes occupy a significant footprint. This motivates research into alternative designs that reduce size while maintaining or improving performance. One such approach is the utilization of nanosensing components[16–18], but they are prone to reliability issues due to stress[19-21]. An alternative approach utilizes the silicon wafer depth for capacitive sensing. While SOI technology enables simple etching, device thickness is currently limited to <200 µm[22–24]. As a result, achieving a larger or similar capacitive plate area in SOI compared to planar Si structures is nearly impossible, making the SOI wafer approach unsuitable for fabricating deep structures[24–28].

Deep silicon etching has become possible owing to recent advancements in Deep Reactive Ion Etching (DRIE) technology. Various authors have exploited this deep etching method[29–34]. The use of a deep reactive-ion etching system to etch to a depth of 600 µm by using a modified Bosch process[35-36]. For even larger etch depths, the use of double DRIE to etch up to 1.4 mm of depth[37]. Additionally, 3D IC technology, which is currently an active topic of research, enables the reduction of the footprint of readout electronics by exploiting the depth of the wafer[38-41]. Therefore, the reduced footprint of both the device and readout IC results in an overall size reduction of the packaged device if the full depth of the Si wafer is exploited. Furthermore, these types of compact devices are required for applications such as mobile devices, the Internet of Things (IoT), and extended reality[3,14].

This study introduces a novel Vertical Sense Mass (VSM) MEMS gyroscope design. Unlike traditional Planar Sense Mass (PSM) designs, the VSM utilizes Deep Reactive Ion Etching (DRIE) to create a deep, compact sense mass. The comparative analysis demonstrates the superior performance of the VSM design over planar configurations in terms of scale factor sensitivity, bandwidth, noise, and overall device footprint. The design details, theoretical equations, design trade-offs, comparative study and finally, experimental validation are studied in subsequent sections.

2. METHODOLOGY

Figure 1(a) – Fig. 1(c) illustrates the proposed Vertical

Received : 04 February 2025, Revised : 03 June 2025
Accepted : 02 July 2025, Online published : 06 November 2025

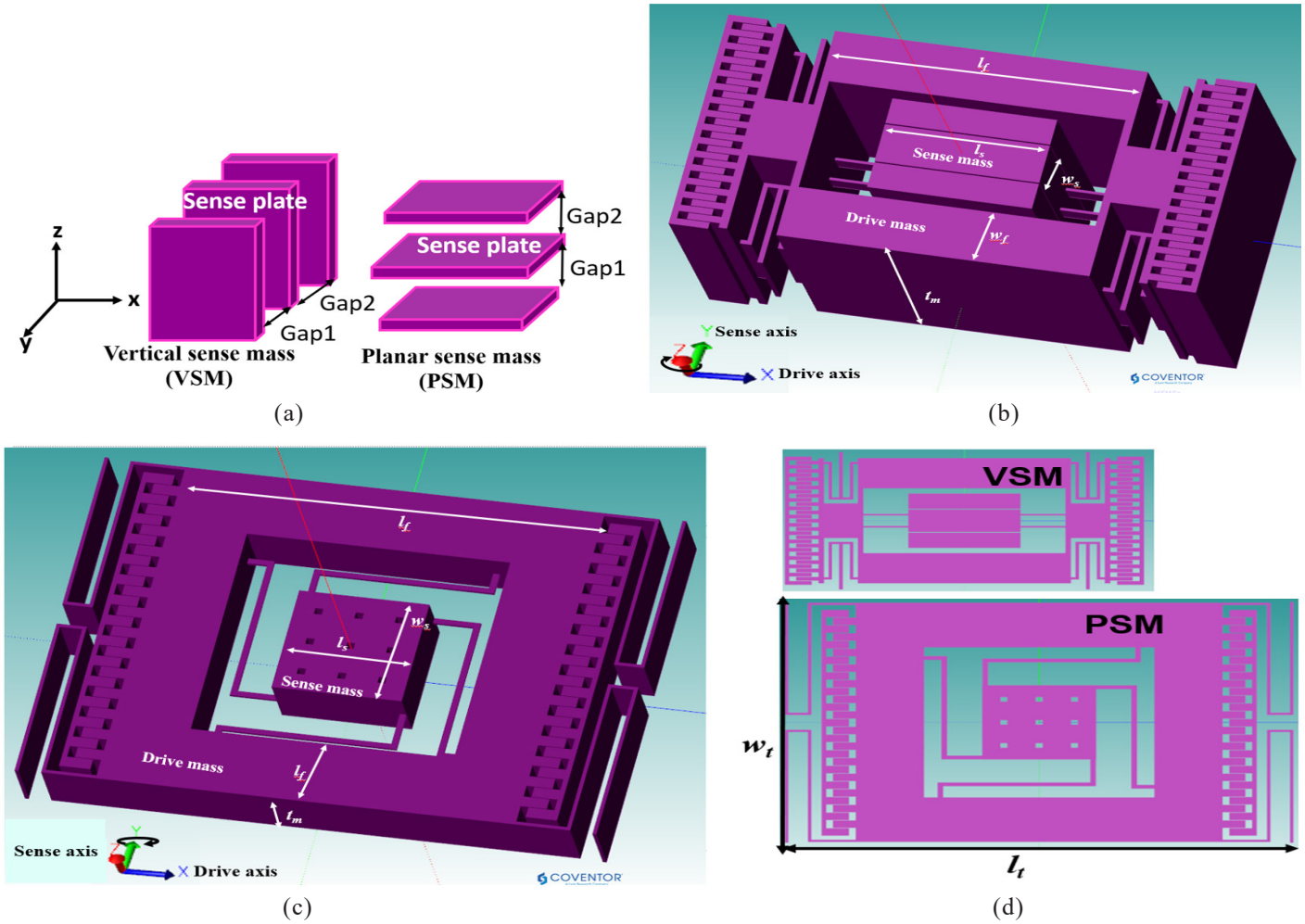

Figure 1. (a) The schematic of Vertical Sense Mass (VSM) and Planar Sense Mass (PSM) structure; (b) Vertical Sense Mass (VSM) design utilizing depth of 500 µm for sense mass structure; (c) Planar Sense Mass (PSM) design that uses a shallow depth of 300 µm for sense mass structure; and (d) Vertical Sense Mass (VSM) and Planar Sense Mass (PSM) design structures on the same scale for footprint comparison.

Sense Mass (VSM) and conventional Planar Sense Mass (PSM) gyroscope designs. The VSM utilizes a deep DRIE-etched structure with the sense mass oriented perpendicularly to the substrate, enabling a more compact design. In the VSM, rotation induces in-plane sense motion, while in the PSM, it induces out-of-plane motion. Both designs measure rotation by sensing the change in gap between moving and fixed structures. Figure 1(d) compares the footprints of the VSM and PSM designs, demonstrating the significant size reduction achieved by the VSM. The proposed VSM design aims to enhance performance metrics such as sensitivity, bandwidth, and noise while minimizing footprint. Theoretical analysis, including mathematical modeling and simulation, will be used to evaluate the performance advantages of the VSM design.

3. ANALYTICAL PERFORMANCE EVALUATION

The performance of the VSM and PSM designs was evaluated based on key parameters: sensitivity, bandwidth, noise, and footprint. The analysis assumed constant angular rate and drive mass oscillation, with negligible sense beam mass and damping. While the VSM exhibits Y-direction deflection due to Coriolis force, and the PSM exhibits deflection perpendicular to it, the analysis uses a consistent coordinate system for simplicity. The VSM design is doable by advanced fabrication techniques and demonstrates improved performance metrics and a reduced footprint compared to the PSM.

The MEMS vibratory gyroscope with a 1-DOF resonator consisting of drive mass m_d, damping coefficient c_d, and spring constant coefficient k_d was set into vibration with amplitude x_0 by applying the electrostatic force F_{Drive} along the x-axis. The amplitude of the vibration x_0 is given[3,41-42].

$$x_0 = \frac{F_{Drive}}{k_d \sqrt{\left[1-\left(\frac{\omega}{\omega_d}\right)^2\right]^2 + \left[\frac{1}{Q_d}\frac{\omega}{\omega_d}\right]^2}} \quad (1)$$

where, $\omega_d = \sqrt{k_d / m_d}$ is the sense-mode frequency, $Q_d = m_d \omega_d / C_d$ is the sense-quality factor, $f_d = \omega_d / 2\pi$ is the drive resonance frequency. The driving electrostatic force F_{Drive} for the proposed comb-actuated structure is given[43]. In both designs, the drive displacement was kept constant for a more meaningful comparison. Owing to the rotation Ω_y in the planar structure, the induced Coriolis displacement of the sense mass m_s with spring constant k_s and damping coefficient C_s in the z-axis[3,41,43].

$$z_o = \Omega_y \frac{m_c \omega_d}{m_s \omega_s^2} \frac{2x_o}{\sqrt{\left[1-\left(\frac{\omega_d}{\omega_s}\right)^2\right]^2 + \left[\frac{1}{Q_s}\frac{\omega_d}{\omega_s}\right]^2}} \quad (2)$$

where $\omega_s = \sqrt{k_s / m_s}$ is the sense mode frequency, $Q_s = m_s \omega_s / C_s$ is the sense quality factor, $f_s = \omega_s / 2\pi$ is the sense resonance frequency and C_s is the sense damping coefficient. m_c is the total mass that generates the Coriolis force and m_s is the sense mass that is excited by the Coriolis force. Further, x_0 indicates that the drive displacement Ω_y represents rotation and y_o represents the sense displacement. The frequency response and subsequent BW of the structure under the application of the rotation rate ω_r are given[44-45].

$$A_{\omega_r} = \frac{x_0 \Omega_y \omega_d}{\omega_r \Delta\omega \sqrt{4\left(1-\frac{\omega_r}{\Delta\omega}\right)+\frac{1}{Q_i^2}}} \times \{1+C_1\}^{\frac{1}{2}} \quad (3)$$

$$C_1 = \frac{\left(1-\frac{\omega_r}{\Delta\omega}\right)^2 + \frac{1}{4Q_i^2}}{\left(1+\frac{\omega_r}{\Delta\omega}\right)^2 + \frac{1}{4Q_i^2}} + \frac{4\left(1-\frac{\omega_r}{\Delta\omega}\right)}{\sqrt{4\left(1+\frac{\omega_r}{\Delta\omega}\right)+\frac{1}{Q_i^2}}}$$

where is the sense amplitude concerning the input angular rate, Q_i is the effective quality factor $Q_i = \Delta\omega \times Q_s / \omega_r$, ω_r is the frequency of the input angular rate $\Delta\omega$ is the difference between the sense and drive frequencies. The sense displacement is plotted against the input frequency, and the frequency at which the response is reduced to 3 dB gives the Bandwidth (BW) of the sensor.

For the MEMS gyroscope, the thermomechanical noise equivalent angular velocity is expressed[45-46]:

$$Noise = \sqrt{\frac{k_B T \omega_s BW}{m_s \omega_d^2 A_{dm}^2 Q_s}} \quad (4)$$

A_{dm} is the area of the drive mass, k_B is the Boltzmann constant, T is the absolute temperature in Kelvin, and BW is the bandwidth.

4. OPTIMIZATION OF SENSE MASS SPRING PARAMETERS FOR VSM AND PSM DESIGN

The VSM design employs flexure springs to ensure linear, predictable response and appropriate resonant frequencies. To suppress undesired twisting modes, the sense mass is suspended by four beams on either side, optimized for the desired in-plane vibration mode. The spring constant for the straight beam of the VSM[47-48].

$$K_{s(vsm)} = \frac{4 E w_{bs} t_{bs}^3}{l_{bs}^3} \quad (5)$$

W_{bs} is the sense spring width? t_{bs} is the sense spring thickness, l_{bs} is the sense spring length, and E is the Young's modulus of silicon. Hence, the effects of spring thickness and length are studied in detail for a proper trade-off and optimization.

4.1 Effect of l_{bs} and t_{bs} on $K_{s(vsm)}$

Spring design significantly impacts VSM performance. Table 1 summarizes the impact of spring dimensions (length, width, thickness) on twisting angle, a critical parameter. Increasing spring length or thickness exacerbates twisting, while increasing width mitigates it. Modal analysis (Fig. 2(b)) confirms these trends. The optimal spring dimensions, determined through analysis, are: thickness (t_{bs}) = 8 µm, length (l_{bs}) = 150 µm, and width (w_{bs}) = 75 µm, resulting in a minimal twisting angle of 0.05°. This optimized design ensures robust performance by minimizing undesired twisting modes while maintaining the desired in-plane vibration for the VSM.

4.2 Effect of l_{bs} and t_{bs} on f_s

Spring dimensions significantly influence the VSM's resonant Frequency (fs). The sense frequency, calculated as $\omega_s = \sqrt{k_{s(vsm)} / m_{s(vsm)}}$ depends on sense mass dimensions (length, width, thickness, and density). Spring dimensions were adjusted to achieve the desired resonant frequency and bandwidth for specific applications. Figure 3 illustrates the variation of fs with spring length and thickness. The sense mass dimensions were optimized considering application requirements and fabrication feasibility.

Figure 3 illustrates the variation of sense frequency with spring length and thickness. The spring dimensions were optimized to achieve the desired resonant frequency and bandwidth for target applications. The VSM design utilizes a flexure-type spring, while the PSM employs a modified crab-shaped spring[22,24,28]. Both designs were optimized to minimize unwanted vibration modes. The VSM design significantly reduces the sense mass footprint, achieving a 30 % reduction in area compared to the PSM. This translates to a 36 % reduction in overall sensor footprint. Modal analysis results, shown in Fig. 4(a) - Fig. 4(d), confirm the desired in-plane drive mode and out-of-plane sense mode vibrations for the VSM and PSM designs, respectively. The VSM design, with its reduced footprint and optimized spring design, demonstrates the potential for significant size reduction and improved performance in MEMS gyroscope technology.

5. COMPARISON OF VSM AND PSM DESIGN PERFORMANCE PARAMETERS

5.1 Sensitivity

The sensitivity of any structure depends on the sense of displacement in response to the produced Coriolis acceleration upon the application of rotation. Figure 5a shows the simulated drive displacements (x_0) at resonant frequencies of 47098 Hz and 3253 Hz for the VSM and PSM designs, respectively. The simulation work has been carried out in CoventorWare 10 software. Coupled DC and AC were applied along the x-axis to obtain a maximum x_0 of 15 µm for both the designs, as shown in this figure. After obtaining the peak drive displacement, the structure was subjected to an angular rotation of 1 rad/s along the z-axis for the VSM design and y-axis for the PSM design (Fig. 1(b) and Fig. 1(c)). Owing to the Coriolis effect, the structure deflects along the y-axis in the VSM design and along the z-axis in the PSM design. Figure 5(b) shows the simulated sense deflections for the VSM and PSM design. The peak deflections in the desired axis at 1 rad/s for the VSM and PSM designs are almost identical at 7.34×10^{-8} m and 7.30×10^{-8} m respectively. The peak twisting amplitude and

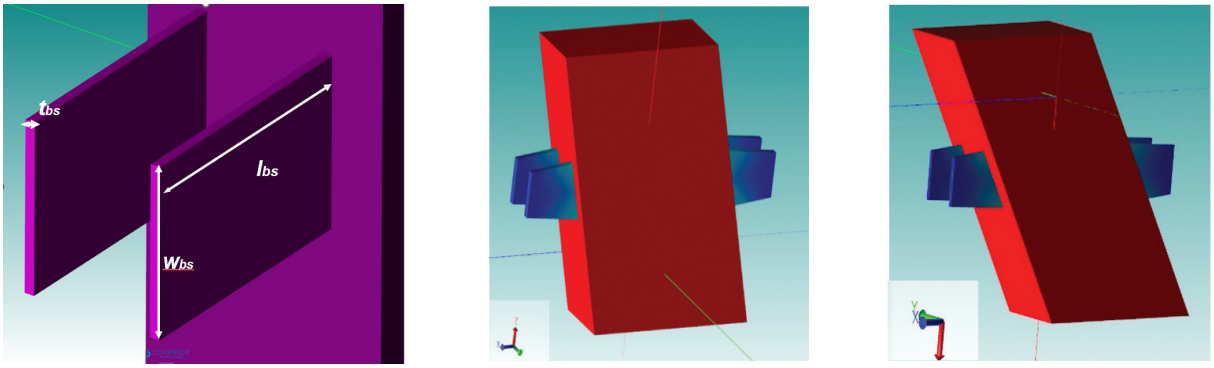

Figure 2. (a) Side view of VSM springs attached to sense mass; and (b) Modal analysis of sense mass for VSM design for two cases, (i) Low twisting and (ii) High twisting.

Table 1. Effect of Sense mass spring length and thickness on sense mode frequency and twisting angle of VSM and PSM

Spring length l_{bs} (µm), spring width w_{bs} (µm)	Spring thickness t_{bs} (µm)	Sense mode 1-frequency f_s of VSM	Sense mode 2-frequency f_s of VSM	Twisting angle of VSM structure (deg)
150 µm, 35 µm	8	32243.5	39202.7	0.86
	10	45052.3	44721.4	2.94
200 µm, 35 µm	8	20937.0	26302.9	2.43
	10	30397.6	29252.2	3.27
150 µm, 50 µm	8	38524.6	65541.0	0.72
	10	53823.7	74141.6	1.35
150 µm, 75 µm	8	47154.8	118875.8	0.05
	10	65871.3	133684.6	0.08

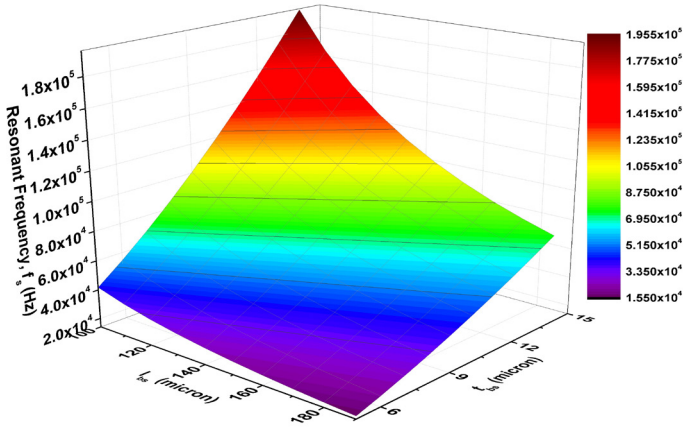

Figure 3. 3d plot showing the variation of sense mass natural frequency with spring length and thickness.

angle for VSM design is 3.21×10^{-18} m and 6.80×10^{-13} deg respectively, which is negligible with respect to the dominating bending mode of vibration of sense mass. Because the results show similar values of sense displacement for the VSM and PSM designs, the performance of the VSM design will be enhanced by utilizing the wafer thickness to reduce the footprint of the device. Furthermore, because the noise has a stronger dependence on ω_d (Eqn. 4), by shifting f_d to a higher value for the VSM design (compared to PSM) while keeping $\Delta\omega$ the same as that of the PSM design, the noise can be reduced in the VSM design and improve the overall PM.

Equation 2 shows that sense displacement depends on mass ratio $M_r=m_d/m_s$ and spring constant ratio $K_r=k_d/k_s$ Optimizing M_r and K_r is crucial for achieving desired resonant frequencies (f_d and f_s) and bandwidth. Drive displacement is kept constant for fair comparison. The VSM and PSM designs are compared at different values of M_r and K_r to assess their impact on performance parameters.

Figure 6(a) illustrates the variation of sense displacement with mass ratio (M_r) at a fixed spring constant ratio (K_r). Here, it is assumed that the structures in both designs vibrate with a constant drive displacement amplitude and rotation rate of 400 °/s. Sense displacement peaks when K_r and M_r are equal, regardless of the design. The VSM design exhibits a maximum sense displacement of 1.15×10^{-2} m at $K_r = 6.9$, while the PSM design achieves a similar value of 1.12×10^{-2} m at $K_r = 7.80$. To comprehensively analyze the influence of both M_r and K_r, a 3D plot depicting sense displacement variation with respect to both parameters is presented in figure 6b. The peak displacement was 1.28×10^{-2} m and 1.18×10^{-2} m for the VSM and PSM designs, respectively. The plot trends for PSM design were similar. For the proposed VSM design, M_r was 7.82, and K_r was 7.80, and for the PSM design M_r was 7.04 and K_r was 6.9 to get the same drive and sense resonant frequencies.

Figure 7 shows the sense displacement at different rotation rates to determine the mechanical sensitivity of both the designs. The rotation rate was varied from 0 to 400 °/s, and the sense displacement was recorded. From the linear curve fitting,

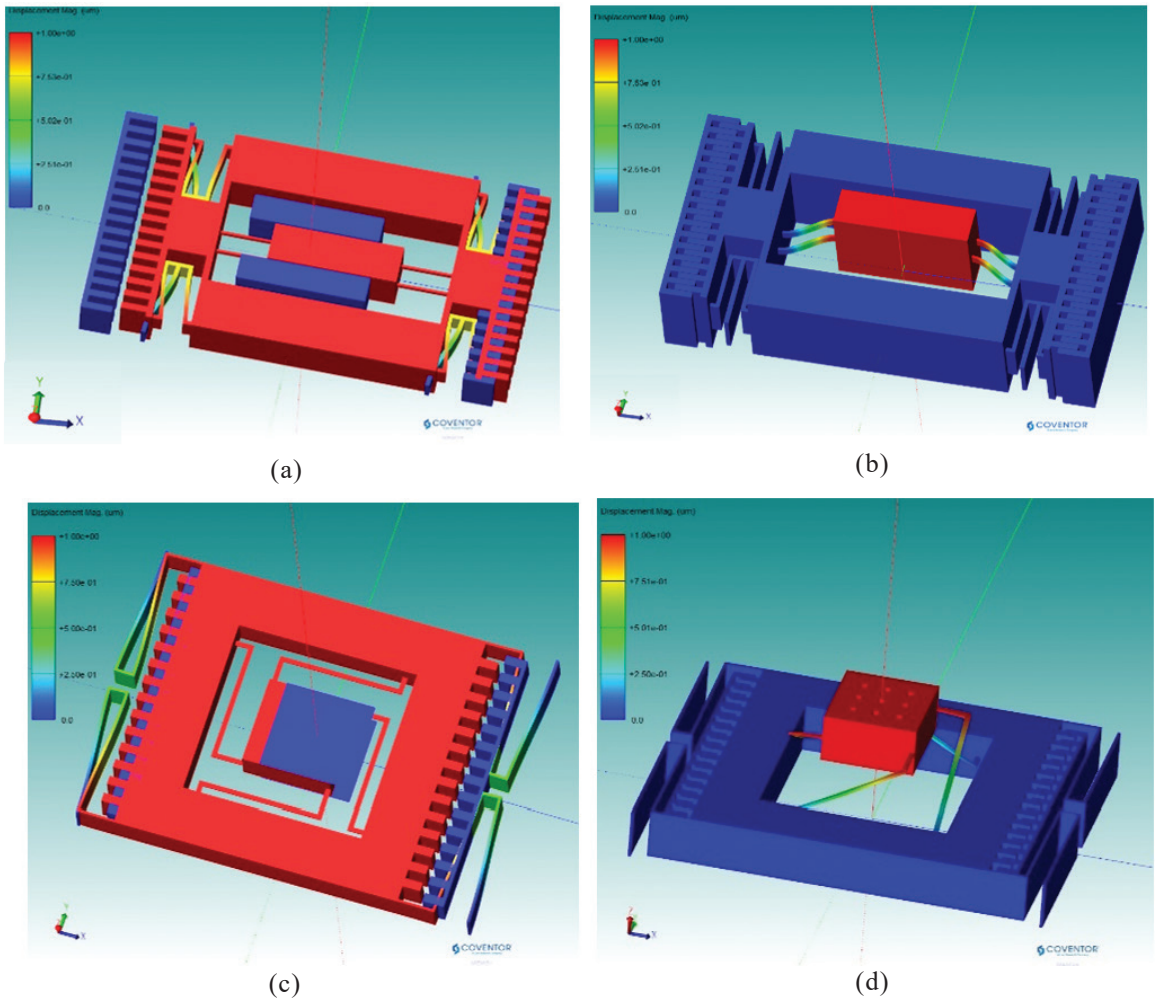

Figure 4. Modal analysis results: (a) Drive mode in VSM design; (b) Sense mode in VSM design; (c) Drive mode in PSM design; (d) Sense mode in PSM design.

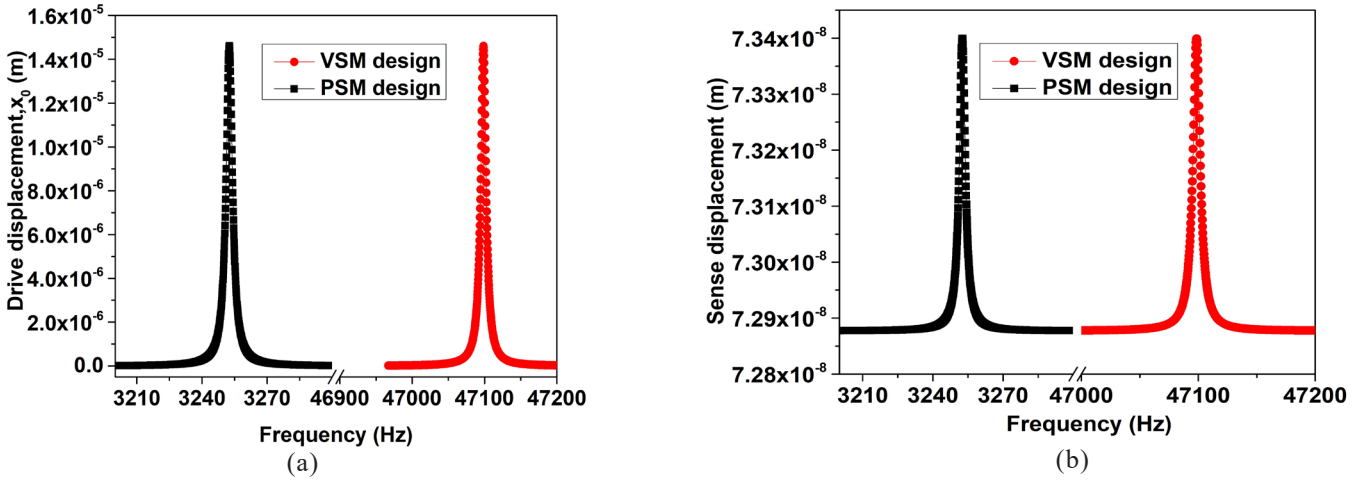

Figure 5. (a) Drive displacement as a function of frequency showing peak at the resonant frequency f_d; and (b) Sense mass displacement as a function of frequency showing peak at the resonant frequency f_s.

the sensitivities for the VSM and PSM design are 9.63×10^{-9} m/deg/s and 9.60×10^{-9} m/deg/s respectively, which shows that VSM is marginally better than PSM. For any structure, if the mass and spring constant ratios are adjusted such that the gap between the drive and sense frequencies is the same, the sensitivity will remain the same and will be independent of the structural dimensions. Thus, it can be concluded that there may not be any reduction in the sensitivity while optimizing and changing the design from PSM to VSM, but there is a gain in the noise and footprint, and hence in the overall performance metric, as will be shown further.

Table 2. Optimized structural parameters for VSM and PSM design

Structural parameters	VSM design	PSM design
Drive and sense mass thickness (t_m)	500 µm	300 µm
Sense beam width (w_{bs}), length (l_{bs}), thickness (t_{bs})	55 µm, 150 µm, 8 µm	25 µm, 950 µm, 15 µm
Sense gap (d)	5 µm	5 µm
Comb fingers length (l_{cm}), width (w_{cm}), width (w_{cm})	100 µm, 50 µm, 2.5 µm	100 µm, 50 µm, 2.5 µm
Drive frequency f_d	47098 Hz	3253 Hz
Sense Frequency f_s	47136 Hz	3291 HZ
Frequency difference (fs - f_d)	38 Hz	38 Hz
Drive mass (m_d), Sense mass (m_s)	1.0×10^{-7} kg, 9×10^{-8} kg	1.1×10^{-6} kg, 1.6×10^{-7} kg
Sense mass foot print	500 µm × 150 µm	500 µm × 500 µm
Total foot print of the device ($l_t \times w_t$)	1510 µm × 860 µm	2232 µm × 1610 µm

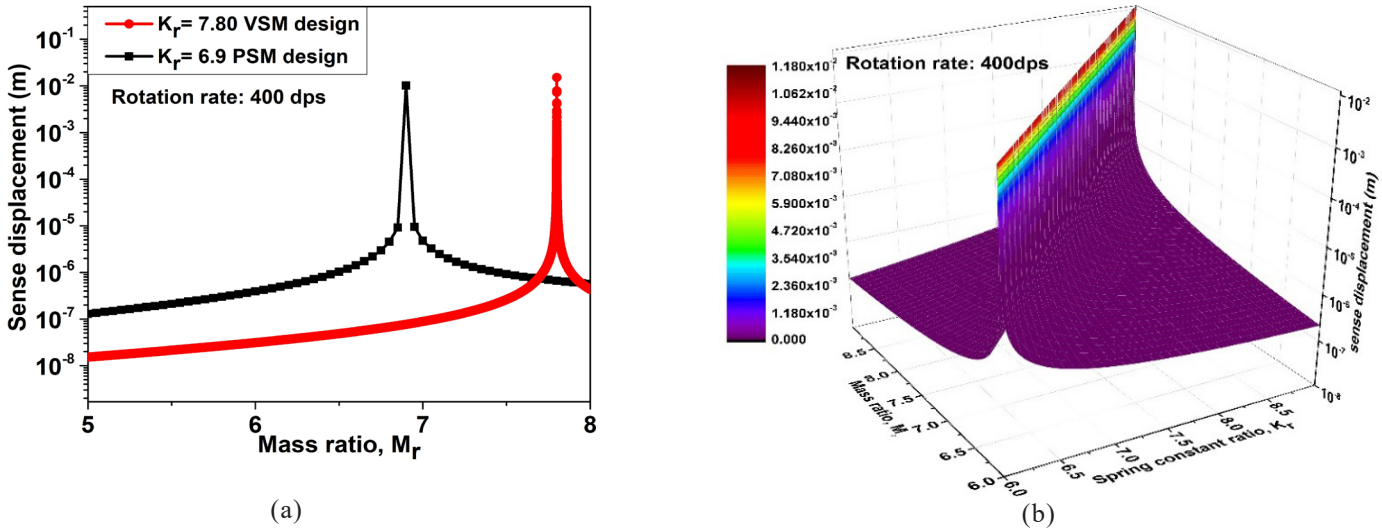

(a) (b)

Figure 6. (a) Sense mass displacement for different M_r at fixed K_r; and (b) The plot of sense displacement at different M_r and K_r for VSM and PSM design.

5.2 Bandwidth (BW)

In this section, we compare the bandwidths of these two designs. As discussed earlier, for a given K_r, M_r can be adjusted M_r to obtain the required resonant frequency guided by a particular BW requirement, or vice versa. Figure 8 shows the 3d plot of the variation in the 3 dB bandwidth with the mass ratio. As can be seen, a V-shaped curve is observed. The pointed end at the bottom of the V-shaped curve shows almost negligible bandwidth; here, M_r, K_r, f_d and f_s are almost the same. As the M_r and K_r values moved far away from one another, the bandwidth increased and the increase was almost linear along the slanted ends of the V-shaped curve. Generally, the structure will have the highest sensitivity at negligible bandwidth, but to get higher bandwidth to measure angular velocity over a wider range of frequencies, one may have to sacrifice the sensitivity. Therefore, it is important to select a gyroscope with the appropriate bandwidth for the intended application. The trend in this plot is the same for both VSM and PSM designs. Figure 9(a) compares the bandwidths of the VSM and PSM designs. The VSM exhibits wider bandwidths (+3 dB: 25 kHz, -3 dB: 73.75 kHz) compared to the PSM (+3 dB: 18 kHz, -3 dB: 51 kHz). This is attributed to the higher resonant frequency of the VSM design. Both designs have similar sensitivity and drive-sense frequency differences. The VSM design, with optimized spring dimensions and a reduced sense mass footprint (30 %), demonstrates improved bandwidth and overall performance.

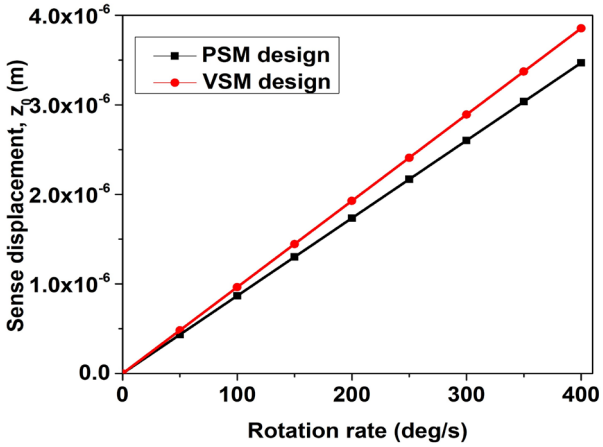

Figure 7. Sensitivity for VSM design (M_r = 7.82, K_r = 7.80) and PSM design (M_r = 7.04, K_r = 6.9) and K_r.

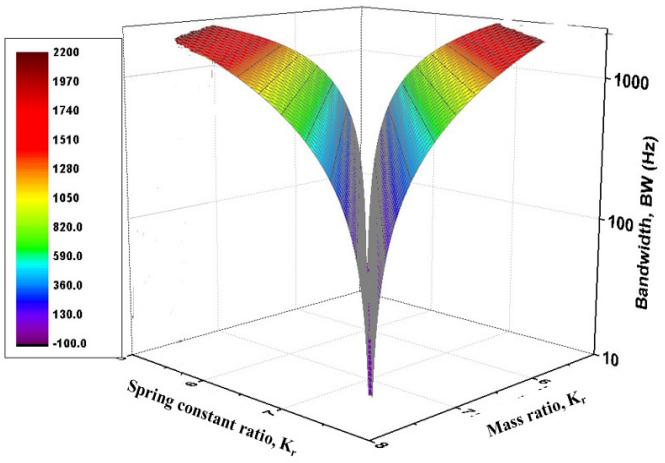

Figure 8. 3d plot of bandwidth variation at diff M_r.

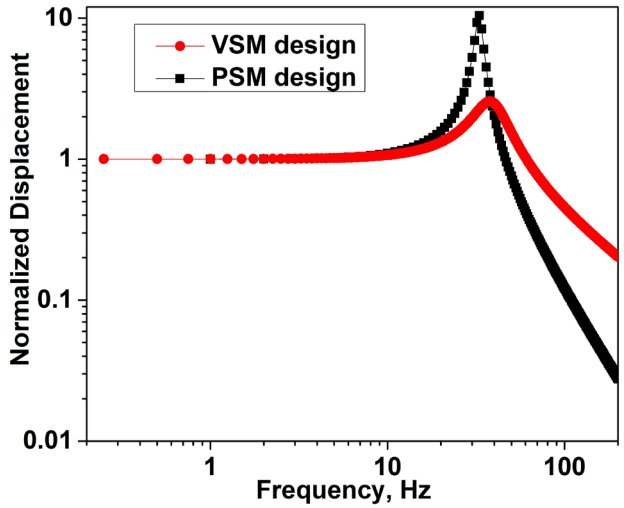

(a)

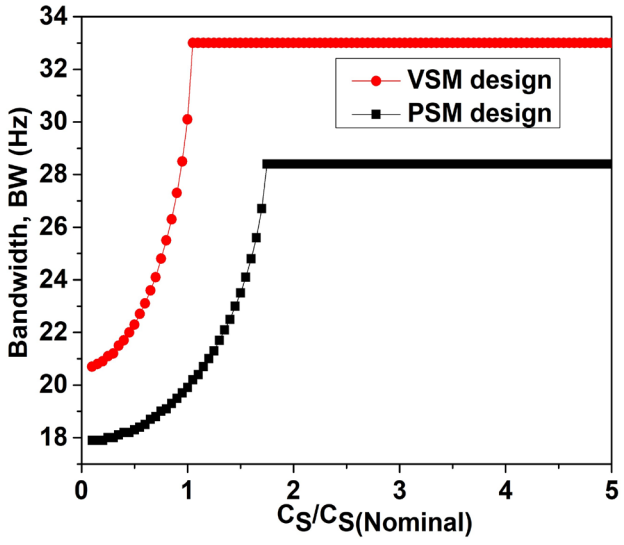

(b)

Figure 9. (a) Normalized displacement for VSM design (M_r = 7.82, K_r = 7.80) and PSM design (M_r = 7.04, K_r = 6.9); and (b) Bandwidth with normalized damping for VSM design (M_r = 7.82, K_r = 7.80) and PSM design (M_r = 7.04, K_r = 6.9).

Figure 9(b) illustrates the impact of damping coefficient (C_s) on bandwidth. For both designs, bandwidth initially increases with C_s but saturates at higher values due to reduced sense amplitude and quality factor. Notably, the VSM design achieves a similar bandwidth (e.g., 29 Hz) at a lower damping coefficient (C_s = 1.05) compared to the PSM (C_s = 1.75). However, at higher damping ratios, the VSM design exhibits more rapid bandwidth saturation.

5.3 Thermomechanical Noise

The VSM design exhibits lower thermomechanical noise compared to the PSM. Noise analysis reveals an inverse dependence on sense mass, drive frequency (ω_d), and drive displacement. The VSM design, with its thicker sense mass (500 µm) and higher resonant frequency to lower the twisting, inherently results in lower noise. Figure 10(a) shows the variation of noise with sense mass thickness, demonstrating

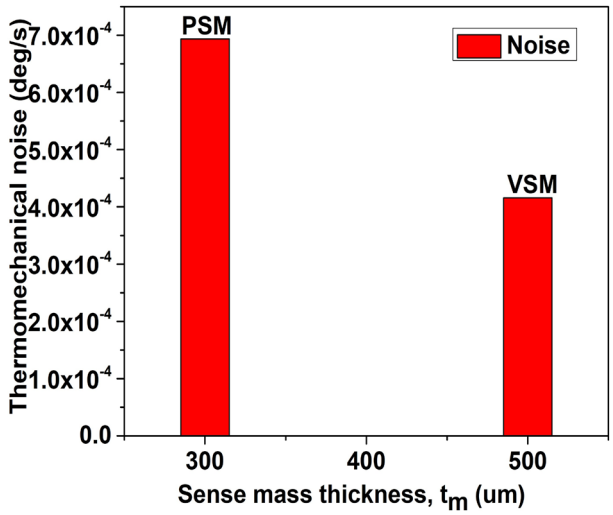

(a)

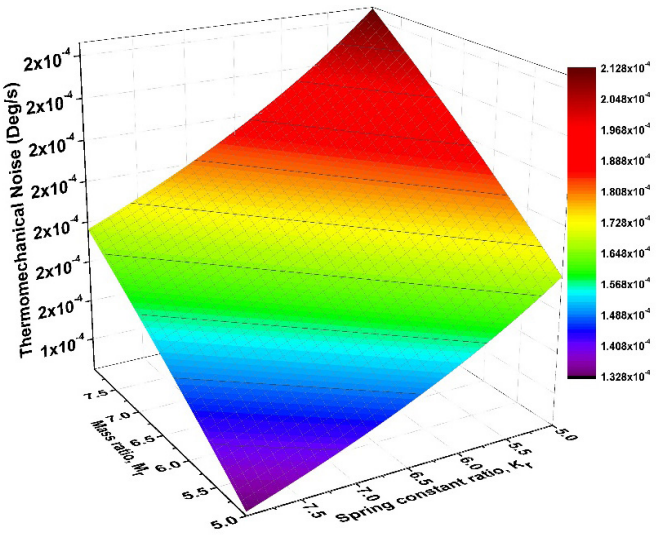

(b)

Figure 10. (a) Thermomechanical noise variation with sense mass thickness; and (b) 3d plot for noise variation at different M_r and K_r for PSM design at 500 µm sense mass thickness.

lower noise for the VSM compared to the PSM. Furthermore, Figure 10b illustrates the dependence of noise on mass ratio (M_r) and spring constant ratio (K_r). While noise varies with M_r and K_r for both designs, the VSM consistently exhibits lower noise levels. For optimized parameters, the VSM achieves 1.7×10^{-4} °/√s noise compared to 6.8×10^{-4} °/√s for the PSM, while maintaining comparable sensitivity and achieving a 36 % reduction in footprint.

Hence, by optimising structural parameters, both VSM and PSM designs achieve comparable sensitivity. However, the VSM design demonstrates superior performance due to its higher resonant frequencies and lower damping, leading to an extended bandwidth. Furthermore, VSM's increased proof mass thickness fundamentally reduces thermomechanical noise. These performance advantages, coupled with a significant 36 % smaller sensor footprint, collectively establish VSM as the more advantageous and efficient design solution.

6. COMPARISON OF THE IMPROVED PERFORMANCE METRIC

New performance metric (PM) is proposed to compare designs, considering sensitivity, bandwidth, noise, and footprint. This metric accounts for the trade-offs inherent in optimizing these parameters. The VSM design, with its reduced footprint and optimized spring dimensions demonstrate superior PM compared to the PSM

$$PM1 = \left[\frac{Sensitivity * BW}{Noise}\right] \quad (6a)$$

$$PM2 = \left[\frac{Sensitivity * BW}{Noise * Footprint}\right] \quad (6b)$$

The resultant values of both the performance metrics should be maximized for a particular design. Different parameters are maximized or optimized for a particular design based on specific applications[27-28,49-50]; however, the newly proposed improved performance metric can facilitate the comparison of different designs on the same platform[17].

The objective was to maximize PM to achieve better performance. A comparison of the performance metrics for the VSM and PSM designs is presented in Table 4. It is evident that the two designs considered for comparison, shown in the above table, have almost comparable sensitivity; however, the VSM design has a higher bandwidth and lower noise parameters, and both have a reduced footprint. If the PSM design is considered at the same higher resonant frequency or bandwidth as the VSM design, the performance metric for the VSM design is higher than that of the PSM design. The PM2 for VSM and PSM is 1090 m Hz/dps^{2}µm^2 and 70.7 m Hz/dps^{2}µm^2, respectively, which is 15.4 times higher than PSM design.

If the footprint is not considered, that is, PM1 for the VSM and PSM design is 1.42×10^{-3} mHz/dps^2 and 2.54×10^{-4} mHz/dps^2, respectively, which is 5.6 times higher than that of the PSM design. Hence, it can be concluded that for VSM, both PM1 and PM2 were higher than those in the PSM design. From a fabrication viewpoint, the VSM design involves a few additional fabrication steps compared to the PSM design. However, these are doable owing to the recent advancements in the silicon fabrication technology of MEMS sensors[20,22,27]. The VSM design, with its improved performance metric and reduced footprint, enables applications in wearable devices, IoT, AR/VR systems, and UAVs, where compact inertial sensors are crucial.

6.1 Comparative Analysis

To validate these findings, different MEMS gyroscope designs were obtained from the literature. Various authors have optimized designs to maximize individual parameters, such as sensitivity, bandwidth, noise, and size. The performance

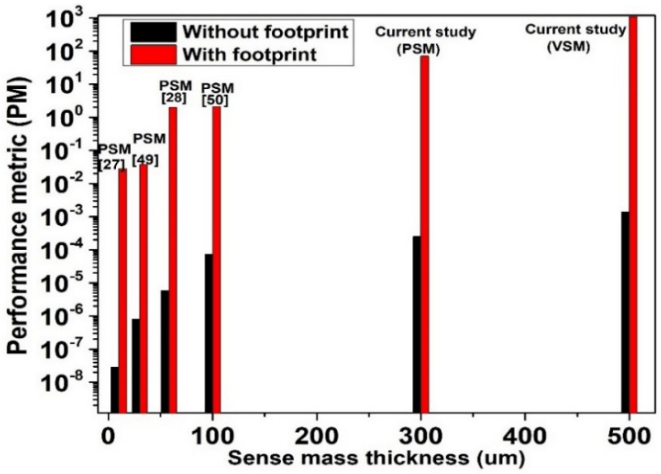

Figure 11. Experimental results of PM at different sense mass thickness for various designs from literature vis-à-vis our proposed design.

Table 3. Comparison of PMs for the proposed VSM design vis-à-a-vis from other designs from literature

Reference	Design type	Sensitivity (m/dps)	Bandwidth (BW)	Footprint (mm×mm)	Sense mass thickness (µm)	Mass, m_s (Kg)	Noise (dps)	PM1 (mHz/dps^2)	PM2 (mHz/dps^{2}µm^2)
26	PSM	4.69e-9	25	1×1	10	3.7e-9	0.0041	2.86e-8	0.0286
48	PSM	1.74e-11	21.6	4.6×4.6	30	2.1e-7	0.00047	8.00e-7	0.0378
27	PSM	1.06e-9	25	2.3×1.3	58	2.3e-8	0.0045	5.89e-6	1.97
49	PSM	1.06e-7	7	5.8×6.0	100	2.5e-6	0.0103	7.20e-5	2.07
Current study	PSM	9.60e-9	18	2.2×1.6	300	1.0e-7	0.00068	2.54e-4	70.7
Current study	VSM	9.60e-9	25	1.51×0.86	500	9.0e-8	0.00017	1.41e-3	1090

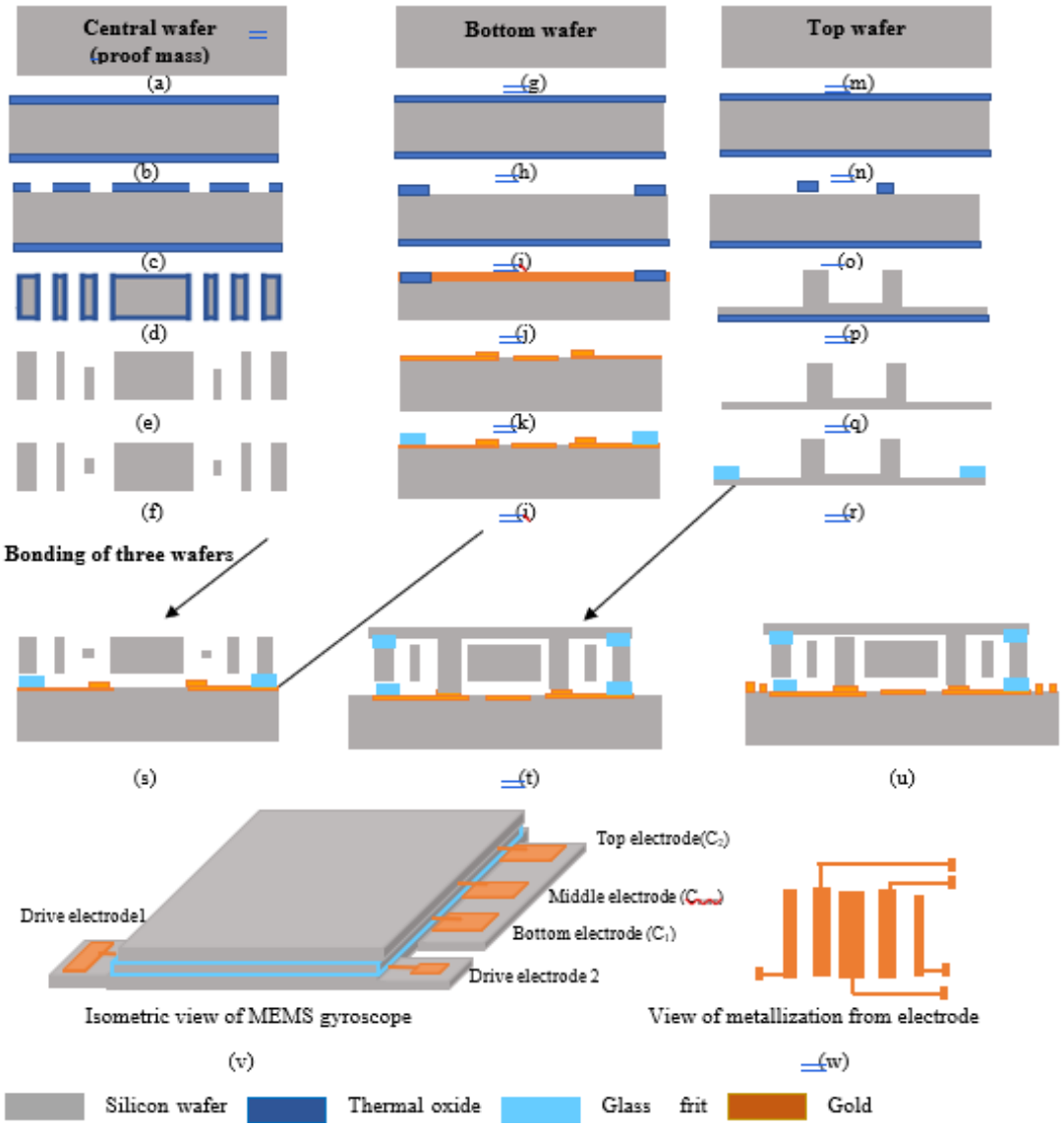

(a)

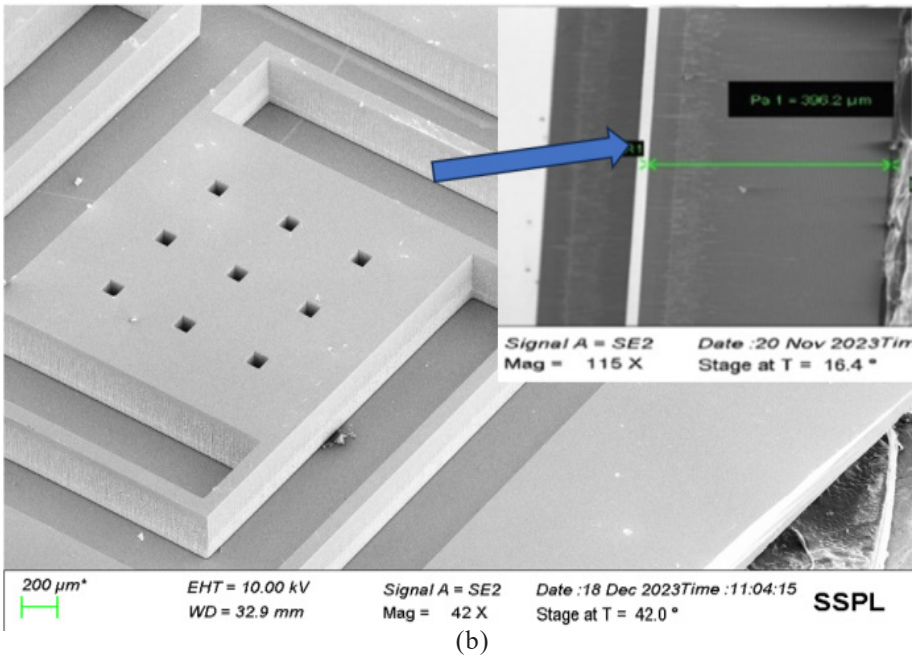

(b)

Figure 12. (a) Fabrication process sequence for the proposed design; and (b) The SEM image of the released structure.

metrics of these designs were compared for a meaningful comparison. Table 3 presents the designs explored in the literature for comparison[26-27,48-49]. The mechanical sensitivity of the sensor in m/dps was noted from individual references. It can be seen from Table 4 that PM1 is 1.41×10^{-3} mHz/dps^2 (without footprint) and PM2 is 1090 mHz/dps^{2}µm^2 (with footprint), which is higher among all. The data were analyzed, and trends between the sense mass thickness and PM1 and PM2 was observed. As there is no continuous variation in the sense mass thickness of the performance metric from the literature, this trend is shown in the histogram plot in Fig. 11.

The plot shows the log of both performance metrics, without a footprint and with a footprint at different sense mass thicknesses. It was observed that both performance metrics improved with an increase in sense mass thickness. When the sense mass thickness was increased from 10 µm to 500 µm, PM1 and PM2 increased by 4.94×10^4 times and 3.80×10^4 times, respectively. Furthermore, as discussed in the introduction the area of the VSM and PSM design is 1.29 mm^2 and 3.59 mm^2. Hence, the area of VSM design achieved using DRIE in MEMS technology is comparable to the 1.2 mm^2 area mentioned by Gadola et al.17 using the NEMS technology.

Hence, the data from the literature is presented to support the analysis considered for comparing the designs, confirming the enhanced performance metric of the proposed VSM design using a thick sense mass.

7. FABRICATION

The proposed fabrication process sequence of the gyroscope is shown in Figure 12a. (i) Central wafer (a)Lapping and polishing, (b)Thermal oxidation (1µm), (c) DRIE etch from front side. (d) Reoxidation, (e) DRIE front side, (f) DRIE back side, (ii) Bottom wafer: (g) Lapping and polishing,(h) Thermal oxide, (i,) Patterned oxide, (j) metal deposition, (k) Metal pattern, (l)Glass frit spinning and patterning, (iii) Top Wafer: (m) Lapping and polishing, (n) Thermal oxide, (o) Pattern oxide, (p) DRIE etch, (q) Oxide remove, (r)Glass frit spinning and patterning, (s) bonding of middle and bottom wafer, (t) bonding with top wafer, (t) Metallization by shadow masking, (v) Isometric view of MEMS gyroscope, (w) View of metallization from electrode.

Device construction necessitates the manipulation of three silicon wafers, each characterized by low resistivity (0.01-0.001 Ω·cm). On the central wafer, the critical device layer is precisely patterned; this involves sequential deposition of multiple masking layers, succeeded by Deep Reactive Ion Etching (DRIE) applied to both its top and bottom faces. Subsequently, this treated central wafer undergoes bonding with two supplementary low-resistivity silicon wafers, which form the upper and lower strata. A comprehensive, step-by-step depiction of the fabrication methodology is provided in Fig. 12, delineating: (i) the stages involved in processing the central wafer (a-f), (ii) the separate fabrication phases for the top (g-l) and bottom (m-r) wafers, and (iii) the final three steps of wafer assembly, comprising the initial bonding of the bottom and central wafers, and then the top wafer to the resulting stack (s-u).

Central Wafer: The initial step, depicted in Fig. 12(a), involves the mechanical thinning and surface planarization of the silicon wafer to attain the target thickness, a parameter readily optimised per established methods[51]. Figure 12(b) then illustrates the deposition of a thermal oxide layer, which functions as a masking layer during the Deep Reactive Ion Etching (DRIE) process. Subsequently, Fig. 12(c) depicts the wafer patterning, accomplished by first defining the desired features via photolithography (PLG)-a process thoroughly described[52-53]-followed by a DRIE step. Figures 12(d) and Fig. 12(e) sequentially show the oxide removal and subsequent re-oxidation. Finally, Fig. 12(f) presents the Deep Reactive Ion Etching (DRIE) of the structure from both front and rear surfaces, a crucial step performed post-photolithography to precisely delineate the beams.

Bottom wafer: Figure 12(g) illustrates the initial preparation of the bottom wafer, where contact areas for two drive electrodes and three sense electrodes are meticulously delineated. A subsequent step, presented in Fig. 12(h), involves thermal oxidation of the wafer, forming a masking layer crucial for later processing. Fig. 12(i) and Fig. 12(j) then detail the patterning of this oxide layer, followed by metallization via sputtering; a secondary patterning step is subsequently applied to selectively increase the metal thickness in specific regions. Following this, Fig. 12(k) depicts the spin-coating of the wafer with a glass frit, which functions as an insulating layer[54]. Subsequently, Fig. 12(l) shows the precise patterning of the applied glass frit. Critically, the controlled thickness of this patterned glass frit layer accurately defines the bonding gap between the top and bottom wafers.

Top wafer: Processing of the top wafer commences with the precise delineation of its sense electrodes. Figures 12(n) and Fig. 12(o) illustrate the wafer's subsequent thermal oxidation and patterning, preparing it for the ensuing etching procedure. Figure 12(p) then details the wafer's patterning using Deep Reactive Ion Etching (DRIE), a step succeeded by the removal of the oxide layer and the application of a glass frit via spin-coating, as visualized in Fig. 12(q) and Fig. 12(r).

Bonding of wafers: Wafer integration is achieved through direct bonding[55]. Figure 12(s) illustrates the initial bonding step, where the central wafer is joined to the bottom wafer. Subsequently, as shown in Fig. 12(t), the top wafer is inverted and precisely aligned onto the previously bonded combination. Figure 12(u) presents the completed bonded stack; electrical contacts are then established from these wafers following a metallization process utilising shadow masking[56].

An isometric perspective of the fully integrated MEMS Gyroscope is provided in Fig. 12(v). The device features two external connections dedicated to the drive displacement mechanism, while the remaining three are allocated for sensing displacement, originating from the top, bottom, and central electrodes. A representative view of the metallization from the middle electrode is presented in Fig. 12(w).

7.1 Deep Reactive Ion Etching (DRIE) Experiment of a Thick Substrate

For the experimental fabrication of robust, thick mass structures, extensive test runs were conducted to optimise the

deep reactive ion etching (DRIE) process. Figure 12b provides a scanning electron microscope (SEM) image of a representative structure, achieved using this optimized DRIE method, which was designed to have a target thickness of 400 µm.

Within the figure's inset, scanning electron microscopy (SEM) measurements of a sidewall indicated a raw thickness of 396.2 µm when the sample was observed at a 16.40-degree mounting angle. After accounting for this non-zero angle, the true sidewall thickness was determined to be 412.1 µm (derived from 396.2 / Cos (16.40)), which closely aligns with the intended 400 µm target. The resulting etch profile demonstrates excellent uniformity, a nearly vertical sidewall angle, and high repeatability. This improved etch selectivity was achieved through the strategic utilization of a composite mask consisting of thermal oxide, nitride, and plasma-enhanced oxide layers.

8. CONCLUSION

This paper introduces an advanced MEMS gyroscope design featuring a vertical sense mass (VSM) architecture, diverging from the conventional planar sense mass configurations commonly reported in the literature. The vertical sense mass configuration leverages deep reactive ion etching (DRIE) techniques to achieve enhanced performance metrics, resulting in a compact sensor footprint. Comparative analyses with traditional planar or crab-leg designs reveal the proposed VSM approach's superior efficacy, demonstrated through theoretical modeling, simulation, and comparative analysis. The tentative process flow to fabricate the structure is discussed, and experimental validation of thick mass with DRIE is also shown. Key performance parameters, including sensitivity, bandwidth, noise, and device footprint, exhibit significant improvements in the VSM design. The reduced form factor of the proposed gyroscope architecture positions it as an ideal candidate for next-generation applications requiring high-performance sensors within a minimal spatial footprint.

REFERENCES

1. Passaro V.M.N, Cuccovillo A, Vaiani L, De Carlo M, Campanella C E. Gyroscope technology and applications: A review in the industrial perspective. Sensors, 2017; 17 (10): 2284. doi:10.3390/s17102284.
2. J. Valldorf, W Gessner. Handbook of advanced microsystems for automotive applications. Springer Berlin Heidelberg; 2007. doi: 10.1007/978-3-540-76989-7.
3. Yunqian He. Handbook of Handbook of Integrated Circuit Industry; 2024. doi:10.1007/978-981-99-2836-1_48.
4. Gill W A, Howard I, Mazhar I, McKee K. A Review of MEMS Vibrating Gyroscopes and Their Reliability Issues in Harsh Environments. Sensors (Basel), 2022; 22 (19): 7405. doi: 10.3390/s22197405.
5. Zhao W, Cheng Y, Zhao S, Hu X, Rong Y, Duan J, Chen J. Navigation grade mems IMU for a satellite. Micromachines (Basel), 2021, 12, 1–12. doi: 10.3390/mi12020151.
6. Weinberg M S. How to invent (or not invent) the first silicon MEMS gyroscope. 2nd IEEE International Symposium on Inertial Sensors and Systems; 2015.
7. Xiao Y, Meng J, Yan H, Wang J, Xin K, Tao T. Research on the Application of MEMS Gyroscope in Inspecting the Breakage of Urban Sewerage Pipelines Water. Sensors (Switzerland), 2023; 15 (13): 2426. doi: 10.3390/w15132426.
8. Wagner J F, Trierenberg A, Wagner J F, G. Bohnenberger J. The Origin of the Gyroscope: The Machine of Bohnenberger. Machines; 2010. doi: 10.1007/978-3-642-39905-3_6,
9. Gill W A, Howard I, Mazhar I, McKee K. Review of MEMS Vibrating Gyroscopes and Their Reliability Issues in Harsh Environments. Sensors (Basel), 2022; 22 (19): 7405. doi: 10.3390/s22197405.
10. Zhang H, Zhang C, Chen J, Li A. A Review of Symmetric Silicon MEMS Gyroscope Mode-Matching Technologie. J Micromachines (Basel), 2022: 13 (8): 1255. doi: 10.3390/mi13081255.
11. Zhanshe G, Fucheng C, Boyu L, Le C, Chao L, Ke S. Research development of silicon MEMS gyroscopes: a review. Microsystem Technologies, 2015; 21 (10): 2053–66. doi: 10.1007/s00542-015-2645-x.
12. Izquierdo, Alberto. Pedestrian detection using a MEMS acoustic array mounted on a moving vehicle. Sensors and Actuators A: Physical, 2024; 376:115586. doi: 10.1016/j.sna.2024.115586.
13. Liu K, Zhang W, Chen W, Li K, Dai F, Cui F, Wu X, Ma G, Xiao Q. The development of micro-gyroscope technology. *J. of* Micromechanics and Microengineering, 2009;19: 113001. doi:10.1088/0960-1317/19/11/113001.
14. Derek K. Shaeffer. MEMS inertial sensors A tutorial overview. IEEE Communications Magazine, 2013; 51 (4): 100-109.
15. A. Jones. Microelectromechanical Systems; A DoD Dual Use Technology Industrial Assessment Microelectromechanical Systems Opportunities*;* 1995.
16. Karimzadehkhouei M. et. al. Silicon Nanowires Driving Miniaturization of Microelectromechanical Systems. Physical Sensors: A Review. Adv. Eng. Mater, 2023; 25 (12): 2300007. doi: 10.1002/adem.202300007.
17. Gadola M, Perna M S, Allieri M, Robert P, Verdot T, Berthelot A and Langfelder G. 600 µdps / √Hz, 1.2 mm^2 MEMS Pitch Gyroscope. Proceedings of 8th IEEE International Symposium on Inertial Sensors and Systems; 2021. doi: 10.1109/INERTIAL51137.2021.9430486.
18. Dellea S, Rey P, Langfelder G. MEMS gyroscopes based on piezoresistive NEMS detection of drive and sense motion. J. of Microelectromechanical Systems, 2017; 26: 1389–99. doi:10.1109/JMEMS.2017.2749121
19. Thapliyal, T. Melong. Study and Analysis of MEMS and NEMS based Gyroscope. Proceedings of the Second

International Conference on Inventive Systems and Control, ICISC, 2018.
20. Larkin K, Ghommem M.A review on vibrating beam-based micro/nano-gyroscope. Microsystem Technologies, 2018; 27: pp- 4157–4181. doi: 10.1007/s00542-020-05191-z.
21. Yang T, Duncan T V. Challenges and potential solutions for nanosensors intended for use with foods. Nat Nanotechnol, 2021; 16 (3): 251–65. doi: 10.1038/s41565-021-00867-7.
22. Bhan R K, Pal R, Dutta S, Yadav I. Development of Unified Fabrication Process and Testing of MEMS Based Comb and Crab Type Capacitive Accelerometers for Navigational Applications. Sensors and Transducers, 2016; 203 (8): 8-15.
23. Kavitha S, Joseph Daniel R, Sumangala K. Design and Analysis of MEMS Comb Drive Capacitive Accelerometer for SHM and Seismic Applications. Measurement J, 2016; 93: 327–339. doi: 10.1016/j.measurement.2016.07.029.
24. Gupta N, Dutta S, Parmar Y, Gond V, Vanjari S R K, Gupta S. Characterization of SOI MEMS capacitive accelerometer under varying acceleration shock pulse durations. Microsystem Technologies, 2021; 27 (12): 4319–27. doi: 10.1007/s00542-021-05227.
25. Kranz M, Hudson T, Ashley P, Ruffin P, Burgett S, Temmen M and Tuck J. Single layer Siliocn-on-insulator MEMS gyroscope for wide dynamic range and harsh environment applications. Proceedings of SPIE-The International Society for Optical Engineering, 2001.
26. Acar C, Shkel A M. An approach for increasing drive-mode bandwidth of MEMS vibratory gyroscopes. J. of Microelectromechanical Systems, 2005; 14 (3): 520–528. doi:10.1109/JMEMS.2005.844801.
27. Alper S E, Akin T. A single-crystal silicon symmetrical and decoupled MEMS gyroscope on an insulating substrate. J. of Microelectromechanical Systems, 2005; 14 (4): 707–17. doi: 10.1109/JMEMS.2005.845400
28. Menon P K, Nayak J, Pratap R. Sensitivity analysis of an in-plane MEMS vibratory gyroscope. Microsystem Technologies, 2018; 24: 2199–213.
29. Owen K J, VanDerElzen B, Peterson R L, Najafi K. High aspect ratio deep silicon etching. Proceedings of the IEEE International Conference on MEMS, 2012; 251–254. doi: 10.1109/MEMSYS.2012.6170138.
30. Herth E, Baranski M, Berlharet D, Edmond S, Bouville D, Calvet L E, Gorecki C. Fast ultra-deep silicon cavities: Toward isotropically etched spherical silicon molds using an ICP-DRIE. Journal of Vacuum Science & Technology B, 2019; 37. doi:10.1116/1.5081503
31. Klaassen E H, Petersen K et. al. A Silicon fusion bonding and deep reactive ion etching: a new technology for microstructures. Sensors and Actuators A: Physical, 1996; 52(1-3): 132-139. doi: 10.1016/0924-4247(96)80138-5.
32. Marty F, Rousseau L, Saadany B, Mercier B, Français O, Mita Y, Bourouina T. Advanced etching of silicon based on deep reactive ion etching for silicon high aspect ratio microstructures and three-dimensional micro- and nanostructures. Microelectronics J, 2005; 36 (7): 673–7. doi: 10.1016/j.mejo.2005.04.039.
33. Roth S, Staufer U, Stebler C, Thí Ebaud P, De Rooij N F. Advanced deep reactive ion etching: a versatile tool for Microelectromechanical Systems. J. of Micromechanics and Microengineering, 1998; 8(4): 272-278. doi: 10.1088/0960-1317/8/4/003.
34. Xu Q, Xiao D, Hou Z, Zhuo M, Li W, Xu X, Wu X. A Novel High-Sensitivity Butterfly Gyroscope Driven by Horizontal Driving Force. IEEE Sensor J, 2019; 19 (6): 2064–2071. doi: 10.1109/JSEN.2018.2886019.
35. Tang Y, Sandoughsaz A, Najafi K. Ultra high aspect-ratio and thick deep silicon etching (UDRIE). Proceedings of the IEEE International Conference on MEMS, 2017; pp. 700–3. doi: 10.1109/MEMSYS.2017.7863504.
36. Tang Y, Sandoughsaz A, Owen K J, Najafi K. Ultra Deep Reactive Ion Etching of High Aspect-Ratio and Thick Silicon Using a Ramped-Parameter Process. J. of Microelectromechanical Systems, 2018; 27 (4): 686–97. doi: 10.1109/JMEMS.2018.2843722.
37. Dyer S, Griffin P F, Arnold A S, Mirando F, Burt D P, Riis E, McGilligan J P. Micro-machined deep silicon atomic vapor cells. J Applied Physics, 2022; 132 (13). doi: 10.1063/5.0114762.
38. Panth S, Kambiz Samadi, Yang Du. High density integration of functional modules using monolithic 3D-IC technology. 18th Asia and South Pacific Design Automation Conference (ASP-DAC), 2013; 681-686. doi: 10.1109/ASPDAC.2013.6509679.
39. Mii Y J. Semiconductor Innovations, from Device to System. Digest of Technical Papers - Symposium on VLSI Technology, 2022; 276–81. doi: 10.1109/VLSITechnologyandCir46769. 2022.9830423.
40. Naeim M, Yang H et. al.Design Enablement of 3-Dies Stacked 3D-ICs Using Fine-Pitch Hybrid-Bonding and TSVs 3DIC. IEEE International 3DIC Conference, 2023. doi: 10.1109/3DIC57175.2023.10155075.
41. Hossam N, Ferguson J. Fast, Accurate Assembly-Level Physical Verification of 3DIC Packages 3DIC. IEEE International 3D Systems Integration Conference, 2023;1-4. doi: 10.1109/3DIC57175.2023.10155000.
42. K. Acar. Handbook of MEMS Vibratory Gyroscopes. Springer, 1979. ISBN 978-0-387-09535-6.
43. Apostolyuk V. Coriolis vibratory gyroscopes: Theory and design. 2016, Springer International Publishing. doi:10.1007/978-3-319-22198-4
44. Patel C, McCluskey P. Modeling and simulation of the MEMS vibratory gyroscope. Inter-Society Conference on Thermal and Thermomechanical Phenomena in Electronic Systems, ITHERM, 2012; 928–33. doi: 10.1109/ITHERM.2012.6231524

45. Bao M.H. Handbook of sensors and actuators and Micro Mechanical. Transducers Pressure Sensors, Accelerometers and Gyroscopes. Elsevier, 2000.
46. Ni Y, Li H, Huang L, Ding X, Wang H. On bandwidth characteristics of tuning fork micro-gyroscope with mechanically coupled sense mode. Sensors (Switzerland), 2014; 14 (7): 13024–45.
doi: 10.3390/s140713024.
47. Lishchynska M, Cordero N, Slattery O, O'Mahony C. Spring constant models for analysis and design of MEMS plates on straight or meander tethers. Sensors Letter, 2006; 4(2): 200–5.
doi: 10.1166/sl.2006.011.
48. Rebeiz G M. RF MEMS: theory, design, and technology. J. Wiley, 2003.
49. Xie J, Shen Q, Hao Y, Chang H, Yuan W. Design, fabrication and characterization of a low-noise Z-axis micromachined gyroscope. Microsystem Technologies, 2015; 21 (3): 625–30.
doi: 10.1007/s00542-014-2068.
50. Xiong X, Dong H. Design and Analysis of a MEMS Vibratory Comb Gyroscope. Conference on Northeast ASEE (The American Society for Engineering Education), Bridgeport, 2009.
51. Shankar Dutta, Manoj Kumar, Surender Kumar, Md Imran, Isha Yadav, Anand Kumar, P. Kumar & Ramjay Pal. Lapping assisted dissolved wafer process of silicon for MEMS structures. Journal of Materials Science: Materials in Electronics, 2015; 25: 1984–1990.
52. Etienne Herth, Maciej Baranski, Djaffar Berlharet, Samson Edmond, David Bouville, Laurie E. Calvet, and Christophe Gorecki. Fast ultra-deep silicon cavities: Toward isotropically etched spherical silicon molds using an ICP-DRIE. Journal of Vacuum Science & Technology B, 2016; 37: 021206.
doi: 10.1116/1.5081503
53. F. Martya , L. Rousseaua , B. Saadanya , B. Merciera , O. Franc¸aisa , Y. Mitab , T. Bourouinaa. Advanced etching of silicon based on deep reactive ion etching for silicon high aspect ratio microstructures and three-dimensional micro- and nanostructures. Microelectronics Journal, 2005; 36: 673-677.
54. G. L. Schnable, W. Kern and R. B. Comizzoli. Passivation Coatings on Silicon Devices. The Electrochemical Society Journal of The Electrochemical Society, 1975; 122 (8).
doi: 10.1149/1.2134402
55. H Moriceau, F Rieutord, F Fournel, Y Le Tiec, L Di Cioccio, C Morales, A M Charvet and C Deguet. A silicon shadow mask for deposition on isolated areas. Journal of Micromechanics and Microengineering, 2000;10 (2).
doi: 10.1088/0960-317/10/2/310

CONTRIBUTORS

Ms Shaveta obtained MTech in Nano Science and Technology from Delhi Technological University and working as Scientist 'F' at DRDO-SSPL, Delhi. He is working in the field of MEMS-based semiconductor devices.
Contribution in the current study, she done simulation, draft writing and compilation of the manuscript.

Dr R.K. Bhan obtained his PhD in Solid State Physics (Microelectronics) from Delhi University. He retired as Scientist 'H(Outstanding)' from DRDO-SSPL, Delhi. He made significant contributions in the field of MEMS sensors, infrared detector development, Charge Coupled Devices (CCDs), CMOS devices, infrared detectors modelling and their characterizations.
Contribution in the current study, he provided motivation, guidance, critical review, and visualization of the work.

Dr Rishu Chaujar working as a Professor in the Department of Applied Physics, in DTU, Delhi. Her areas of interest are semiconductor device modeling & simulation: Analysis of novel device.
Contribution in the current study, she offered guidance, critical review, and gave final approval for the manuscript.